Supersonic Boundary Layer Interactions with Various Micro-Vortex Generator Geometries

S. Lee[1] and E. Loth[2]
University of Illinois at Urbana Champaign

Various types of micro-vortex generators (µVGs) are investigated for control of a supersonic turbulent boundary layer subject to an oblique shock impingement, which causes flow separation. The micro-vortex generators are embedded in the boundary layer to avoid excessive wave drag while still creating strong streamwise vortices to energize the boundary layer. Several different types of µVGs were considered including micro-ramps and micro-vanes. These were investigated computationally in a supersonic boundary layer at Mach 3 using Monotone Integrated Large Eddy Simulations (MILES). The results showed that vortices generated from µVGs can partially eliminate shock induced flow separation and can continue to entrain high momentum flux for boundary layer recovery downstream. The micro-ramps resulted in thinner downstream displacement thickness in comparison to the micro-vanes. However, the strength of the streamwise vorticity for the micro-ramps decayed faster due to dissipation especially after the shock interaction. In addition, the close spanwise distance between each vortex for the ramp geometry causes the vortex cores to move upwards from the wall due to induced upwash effects. Micro-vanes, on the other hand, yielded an increased spanwise spacing of the streamwise vortices at the point of formation. This resulted in streamwise vortices staying closer to the floor with less circulation decay, and the reduction in overall flow separation is attributed to these effects. Two hybrid concepts, named "thick-vane" and "split-ramp", were also studied where the former is a vane with side supports and the latter has a uniform spacing along the centerline of the baseline ramp. These geometries behaved similar to the micro-vanes in terms of the streamwise vorticity and the ability to reduce flow separation, but are more physically more robust than the thin vanes.

Nomenclature

a	=	speed of sound
α	=	total pressure recovery factor
A_{sep}	=	separation area
B	=	blending function
BR	=	baseline micro-ramp
BV	=	baseline micro-vane
β	=	frictional velocity ratio
CFL	=	Courant-Freidrichs-Lewy number
D	=	width of the computational domain
δ	=	boundary layer thickness
δ_{ref}^{*}	=	displacement thickness at inviscid shock location but with no shock effects
dt	=	time increment for integration
dx	=	spatial increment in streamwise direction
dy	=	spatial increment in normal direction
dz	=	spatial increment in spanwise direction
Γ	=	circulation induced by vortex generators
h	=	micro-ramp height

---

[1] Research Assistant, Department of Aerospace Engineering, Urbana, IL, 61801, Member AIAA.
[2] Professor, Department of Aerospace Engineering, Urbana, IL, 61801, Associate Fellow AIAA.

H	=	incompressible shape factor
η	=	wall normal coordinate normalized by boundary layer thickness
HHR	=	baseline micro-ramp with reduced height by half
HWR	=	baseline micro-ramp with reduced width by half
K	=	spatial average of time-averaged turbulent kinetic energy
κ	=	Von Karman constant
L	=	length of the computational domain
M	=	Mach number
NR	=	no micro-ramp
p	=	time-averaged pressure
P	=	spatial average of time-averaged pressure
P_o	=	total pressure
SR	=	BR split at the centerline
SBLI	=	shock boundary layer interaction
Δt	=	time step
T	=	temperature
τ	=	integration time
τ^*	=	integration time normalized by the freestream flow convection time
TV	=	thick vane
u	=	instantaneous streamwise velocity
u'	=	streamwise fluctuation velocity
U	=	average streamwise velocity
U_τ	=	frictional velocity
υ_ω	=	kinematic viscosity at wall
v	=	normal velocity
w	=	spanwise velocity
ω_{max}	=	maximum streamwise vorticity in a vortex core
x	=	streamwise distance
Δx	=	streamwise length of computational cell
ξ	=	i direction in computational domain
y	=	normal distance relative to solid-wall
Y	=	trajectory of ω_{max} in y
ψ	=	j direction in computational domain
z	=	spanwise distance relative to center of domain
Z	=	trajectory of ω_{max} in z
ζ	=	k direction in computational domain

Superscripts

$\overline{}$	=	time-averaged
$+$	=	dimension in wall units
$*$	=	dimension normalized by δ_{ref}^*
$**$	=	dimension normalized by h
inner	=	boundary layer inner region
outer	=	boundary layer outer region

Subscripts

dom	=	domain
f	=	total integration time required for final convergence
i	=	initial value
∞	=	freestream value
inlet	=	upstream plane used as input for recycling
int	=	total integration time
max	=	maximum

MP   =   measuring plane
recycle=   downstream recycling plane
SI   =   theoretical shock impingement location
TE   =   µVG trailing edge location

I.   Introduction

Shock wave interaction with a turbulent boundary layer can result in significant adverse effects to the flow which can degrade the performance of supersonic inlets. Examples of adverse effects include shock induced flow separation which consequently causes an increase in the boundary layer thickness and stagnation pressure loss. Flow control application for shock boundary layer interaction remains an important technology that needs further exploration. A popular flow control method is to bleed the flow at the shock impingement to suppress separations which thins the boundary layer and increases the pressure recovery. However, a bleed has a significant penalty cost of removing up to tenth of the incoming mass flow[1] in order to work properly. This requires larger inlets to compensate for the lost mass flow which can lead to weight increase and drag. Therefore, a device that can reduce or even completely eliminate bleeding is highly desirable. Vortex generators (VGs) have been used in many passive flow control applications such as on wings at transonic speeds[2]. Although very effective in delaying or eliminating flow separation, the parasitic drag is large due to the device height which is close to the boundary layer thickness. Holmes *et al.*[3] suggested that smaller VGs can produce benefits similar to those of traditional VGs while having greatly reduced parasitic drag. In particular, these smaller VGs are characterized by heights less than the boundary layer thickness and have been referred to as "low-profile" or "micro" VGs. A recent study by Anderson[4] indicated that a micro VG in the form of 'micro-ramp' yielded improvements in inlet performance similar to those gained using a traditional boundary layer bleed. He optimized the size and relative length scales based on the downstream incompressible shape factor using RANS numerical methods. However, Ghosh *et al.*[5] found some significant differences between RANS and experimental results while their less-empirical hybrid LES/RANS approach yielded better agreement with the downstream experimental data such as flow recovery. Similarly, Lee and Loth[6] used Monotone Integrated Large Eddy Simulations (MILES) approach and found substantial improvements compared to RANS results. They also found that the reducing the size of the micro-ramps and placing them closer to the impinging shock location allowed reduced flow separation area at the impinging shock and increased pressure recovery downstream. This indicates that the optimum µVG design may be dependent on flow conditions and may require capture of the unsteady large-scale structures.

In this study, our aim is to understand the physics of the interaction between the shock wave, the turbulent boundary layer and the counter-rotating vortex pair generated from the flow control device. The MILES approach incurs less empiricism than the RANS allowing one to obtain detailed information of the fluid physics. We seek to understand how the development of the vortices differs between various device geometries and compare that to previous subsonic measurements[7]. Furthermore, we hope to understand the evolution of the turbulent structures passing over the µVGs and the impact of the oblique shock. Finally, we wish to determine the effect of different geometries of the µVGs on flow separation and downstream boundary layer properties including stagnation pressure recovery. To be consistent with validation data from Air Force Research Laboratory at Wright Patterson (AFRL)[6], we investigate a Mach 3 turbulent boundary layer with $Re_{\delta*}$ = 3,800 with an 8° oblique impinging shock.

II.   Numerical Methodology

Large Eddy Simulation (LES) is used to provide high spatial and temporal resolution for unsteady turbulent flow with little empiricism. Turbulence modeling for sub-grid stress is neglected, which is the MILES approach where the artificial dissipation in the numerical scheme acts as the sub-grid stress model. Near the wall of a boundary layer, this approach employs only physical viscosity (and a near-wall grid density is close to that needed for Direct Numerical Simulation). In the outer portion of the boundary layer, the flow is virtually inviscid such that turbulence modeling is also unnecessary. Previous studies have shown that the MILES approach for a supersonic turbulent boundary layer simulation gives close agreement to a Smagorinsky sub-grid stress model.[8] The frame work of the code is based on WIND (developed at AEDC, NASA Glenn), which is a finite-volume solver for compressible flows. The inflow boundary conditions have been modified to generate turbulent boundary layer flow and data collection subroutines were added to obtain time-averaged data. A third-order upwind scheme is used with Min-mod TVD to capture high-fidelity shocks and turbulent structures with high resolution MILES grid. For time

integration, a second-order approximate factorization scheme[9], a class of Alternating-Direction Implicit scheme, is employed with Newton sub-iteration to improve temporal accuracy. Time step is based on $dt=CFL\Delta x/(a_\infty+U_\infty)$, where Δx is the smallest streamwise cell length and a_∞ and U_∞ is the speed of sound and streamwise velocity at freestream conditions. Courant number (CFL) of 0.4 was based on stability constraints, but was small enough to ensure time-step independence. The computational resource for the MILES results was provided by the National Center for Supercomputing Applications at the University of Illinois where approximately 10,000 unit hours computing time was required.

i. Rescaling-Recycling

The rescaling-recycling method for compressible boundary layer flows is based on that of Urbin *et al.*[8, 10] which is a computationally efficient method of generating a turbulent inflow condition by avoiding a computational domain for the spatial development from laminar flow through transition to turbulent flow. An instantaneous flow field at a given downstream location is rescaled to fit the frictional velocity and the boundary layer height for a targeted flow field upstream. The upstream and downstream planes are denoted respectively as the "inlet station" and the "recycle station" where the distance between the planes should be longer than 1000 wall units[10]. For a fully turbulent boundary layer flow, the boundary layer profile can be decomposed into two layers, namely the "inner" and the "outer" layer. The time and spanwise averaged streamwise velocity U is defined as

$$U = \frac{1}{\tau_{int} D} \int_0^D \int_0^{\tau_{int}} u \, dt \, dz \tag{1}$$

This can be used to evaluate the inner layer profile which is related to the law of the wall:

$$U_\tau^2 = \nu_w \left[\frac{\partial U}{\partial y} \right]_{y=0} \tag{2}$$

$$U^{inner} = U_\tau(x) \left[\frac{1}{\kappa} \ell n(y^+) + C \right] \tag{3}$$

In these expressions, u is the instantaneous streamwise velocity, D is the width of the domain, τ_{int} is the total integration time required for convergence. y^+ is the wall unit in the normal direction of the wall, κ is the von Karman constant and C is the second inner-wall empirical constant. U_τ is the frictional velocity which is the gradient of the average streamwise velocity with the kinematic viscosity at the wall, ν_w, as defined in Eq. 2. Since the mean wall shear stress will change over the computational domain owing to spatial development, the inner profiles can be computed at the inlet station using the following equation.

$$U_{inlet}^{inner} = \beta U_{recycle}^{inner}(y_{inlet}^+) \tag{4}$$

where $\beta = U_{\tau, inlet} / U_{\tau, recycle}$ is the frictional velocity ratio which is specified *a priori*. Note that $U_{recycle}^{inner}$ must be modified to the y^+ coordinate system at the inlet station from its original coordinate. The outer layer profile obeys the velocity defect law which is also dependant on the frictional velocity.

$$U_\infty - U^{outer} = U_\tau(x) f(\eta) \tag{5}$$

where $\eta = y/\delta$ and δ is the boundary layer thickness, and the inlet value of δ is specified *a priori*. Using the frictional velocity ratio, upstream velocity profile at the inlet station for outer layer can be computed by the following equation,

$$U_{inlet}^{outer} = \beta U_{recycle}^{outer}(\eta_{inlet}) + (1-\beta)U_\infty \tag{6}$$

where $U_{recycle}^{outer}$ is interpolated to the η coordinate system at the inlet station. Both the inner and the outer layer profiles for the fluctuating velocity terms at the inlet station are obtained by using the frictional velocity ratio, β.

$$u_{inlet}^{'inner} = \beta u_{recycle}^{'inner}(y_{inlet}^+, z, t) \tag{7}$$

$$u_{inlet}^{'outer} = \beta u_{recycle}^{'outer}(\eta_{inlet}, z, t) \tag{8}$$

Combining the average and the fluctuating terms, the instantaneous velocity profile at the inlet station that is "rescaled and recycled" can be computed using the blending function.

$$u_{inlet} = (U_{inlet}^{inner} + u_{inlet}^{'inner})[1 - W(\eta_{inlet})] + (U_{inlet}^{outer} + u_{inlet}^{'outer})W(\eta_{inlet}) \tag{9}$$

where the blending function[11] is defined as

$$B(\eta) = \frac{1}{2}\left[1 + \tanh\left(\frac{4(\eta - 0.2)}{0.6\eta + 0.2}\right) / \tanh(4)\right] \tag{10}$$

This method applies to other primitive variables such as the normal velocity, v, spanwise velocity, w, and the temperature, T. The pressure at the inlet is assumed constant due to negligible fluctuations[12], thus the density field at the inlet station can be computed directly from the rescaled temperature by using the equation of state. More details on the recycle method can be found in Urbin et al.[8, 10] and Lee et al.[6].

ii. μVGs and Computational Grid

The baseline micro-ramp (BR) with a height of h is shown in Fig. 1a where the dimensions are based on the optimization results from the RANS-based Anderson study [4]. Different dimensions, such as reducing the height by half (HHR) in Fig. 1b and the width by half (HWR) in Fig. 1c, are additionally investigated, as well as a split micro-ramp (SR) shown in Fig. 1d. Furthermore, micro-vanes are examined where the baseline vanes (BV) and thick vanes with side support (TV) are shown in Fig 1e & f, respectively, both of which have the same height as the baseline micro-ramp. The top-view of the devices is shown on the right column where the sweep angles and the heights can be seen. In all cases (including the half-width ramps), the spacing between the adjacent μVG based on the centerlines of the device is 7.5h. The lower sweep angles of the vanes are similar to that of the half-width ramp (HWR). Note that the vane dimensions were based on Ashill et al.[7] to allow comparison to their experimental data set, which was obtained for a single pair of vanes at a low-speed subsonic condition (Mach number close to 0.08). This experimental data set also included a micro-ramp with a similar sweep angle, length and height as that of the vanes.

The computational grid shown in Fig 2a is a scaled version of the test section of a wind tunnel at AFRL which included a downstream measuring plane (MP). The flow domain is dimensioned in this figure in terms of a reference displacement thickness, denoted as δ_{ref}^*. The reference displacement thickness of the boundary layer is that measured for a clean flat plate flow (i.e. no shocks and no micro-ramps) but at the position of the theoretical inviscid shock (x_{SI}). The ratio of the baseline micro-ramp's height, h, to the displacement thickness is 3.19 $(h=3.19\delta_{ref}^*)$ based on Anderson[4]. The length and the width of the grid is $312\delta_{ref}^*$ and $23.7\delta_{ref}^*$, respectively. The spanwise coordinate z is 0 at the centerline and $z^*=z/\delta_{ref}^*$. The normal coordinate y is zero at the floor such that the height of the grid varies from y of $86.3\delta_{ref}^*$ to $61.1\delta_{ref}^*$ at the entrance and the exit of the domain and $y^*=y/\delta_{ref}^*$. The streamwise distance was normalized by the reference displacement thickness and centered at the theoretical shock impingement location (x_{SI}) so that $x^*=(x-x_{SI})/\delta_{ref}^*$. The micro-ramp trailing edge is located at $57\delta_{ref}^*$ upstream of the inviscid shock impingement location (i.e. $x^* = -57$). The full domain is decomposed into 11 zones for parallelization

to increase computational efficiency where each interfacing zones are abutting grids. An enlarged side view of the grid for the baseline micro-ramp (Fig. 1a) is shown in Fig. 2b.

The rescale-recycling zone whose length is $29.5\delta_{ref}^*$ generates turbulent boundary layer flow at the inflow of the domain which is followed by an oblique shock induced by the 8° wedge on the ceiling as shown in Fig. 2. The μVGs are placed approximately at the mid-point between the inflow and the outflow of the domain which is upstream of the inviscid shock impingement region. The shock is then reflected from the impingement location and convects downstream passing through the outflow plane at x*=102. Data measurement to assess the μVG performance is conducted at the measuring plane (x_{MP}) which is based at x*=86.2. Periodic boundary conditions are imposed on the side walls of the domain to represent arrays of μVGs in the spanwise direction which would make the spacing between the adjacent μVG equal $23.7\delta_{ref}^*$. Slip and no-slip conditions are imposed on the ceiling and the floor of the domain, respectively, where the outflow conditions are based on zero order pressure extrapolation. The grid stretching ratio (division of two consecutive cell lengths) in the normal direction to the wall is 1.15 where the first grid point normal to the wall is at $y^+ = 1$ (based on the shear stress at the inlet station of rescale-recycle zone). The streamwise and the spanwise grid spacing correspond to x^+ of 28 and z^+ of 13 whereby the total number of grid points is 3.2 million nodes, which is denoted as the baseline grid (BG). Finer grid spacing was necessary in the zones that surround the μVG in order to conform to the boundaries of the geometry, which is shown in vertical slice of the grid above the μVG in Fig. 2.

iii. Validation, Mean Flow Convergence and Grid Independence

The mean MILES streamwise velocity at x_{MP} was compared to an experimental data obtained by AFRL (also at a similar Reynolds number of 4,000 based on δ_{ref}^*) in Fig. 3a using the baseline grid. The No Ramp (NR) flowfield included the oblique shock wave but no control device. For the mean velocity, the time averaging based on Eq. 1 employed a time period of $\tau^*=4$ where $\tau^*=\tau_{int}/\tau_{dom}$. τ_{dom} is defined by $\tau_{dom}=L/U_\infty$ and where L is the streamwise length of the domain ($312\ \delta_{ref}^*$) and U_∞ is the freestream velocity. This quantity represents a time scale for the fluid to convect through the entire domain, i.e. a single time-sweep. Good agreement is found for the velocity profile (especially compared with RANS predictions[6]), though the shear stress was somewhat under-predicted. A similar comparison was made for the oblique-shock case where the baseline micro-ramp (BR), included in Fig. 3b, where it can be seen that the fuller boundary layer measurements with the control device are consistent with the trends predicted by MILES.

To examine effects on time-averaging (used in Eq. 1) and on spatial resolution, the micro-ramp case of Fig. 3b was recomputed two more times: once with an increased integration time and again with an increased grid resolution. For the former, temporal convergence of the velocity profile was examined by extending the averaging interval by $\tau^*=8$ and negligible differences were found as shown in Fig. 3b. Decreasing the time-step by a factor of two to check temporal resolution also yielded even smaller differences (which are not shown). The grid resolution study was performed by increasing grid points of the baseline grid by 30 percent in each of the computational coordinate directions (ξ, ψ and ζ). This resulted in an increase in the total number of nodes by a factor of 2.2 where the new grid is defined as the dense grid (DG). The predictions based on the DG integrated over $\tau^*=4$ are also shown in Fig. 3b and only small differences in the mean velocity profiles were found compared to the other numerical and experimental results, where similar results were found with the stagnation pressure profile[6]. Therefore the flow solution from the baseline grid with the time scale of τ*=4 for averaging is deemed sufficiently resolved and reasonably predicts the downstream velocity profile. This gives confidence in the technique to predict the flow interaction for other micro vortex-generator devices for which no experimental data is available.

III. Results

In the present study we consider a Mach 3 turbulent boundary layer at $Re_{\delta*}$ of 3,800 (based on δ_{ref}^*), where the freestream pressure and the temperature are 7076 N/m^2 and 582.3 K, respectively. This flow is subjected to an 8° oblique shock. Different types of μVGs from Fig. 1 are placed upstream of the shock interaction with the boundary layer. To characterize the impact, the evolution of the turbulent structures is first discussed followed by that for the evolution of the mean streamwise velocity in terms of streamwise, transverse, and spanwise distributions. Next, the streamwise development of a spatially-averaged kinetic energy and streamwise vorticity is investigated, where the latter is compared to previous measurements in low-speed sub-sonic flow[7]. Finally, the impact of the devices on

downstream stagnation pressure recovery, displacement thickness and shape factor are considered, along with the net change in separation area.

i. Turbulent Boundary Layer

Instantaneous density iso-surfaces and streamwise velocity contours at y^+ of 5 without the flow control device are shown in Fig. 4a & b. In terms of overall gas dynamics, Fig. 4a shows that the oblique shock wave propagating downward (shown in green) followed downstream by an expansion wave generated from the trailing edge of the shock wedge which also propagates downward (shown in green). The reflected shock from the turbulent boundary layer (shown in yellow) moves upwards and interacts with the expansion wave. It should be noted that the incoming oblique shock wave is two-dimensional while the reflected wave contains significant spatial undulations (and was found to be unsteady). These figures also show the evolution of the coherent structures convecting through the shock. As the shock impinges on the boundary layer, the shapes of the structures just downstream of the shock become more vertically pronounced (Fig. 4a). This is due, in part, to the boundary layer thickening and the adverse pressure gradient. The results also show a reduced aspect ratio of the structures, though they begin to relax towards the pre-shock aspect ratios further downstream (Fig. 4a & b). The reduced aspect ratio and associated reduced coherence of the structures in the streamwise direction near the shock may be attributed to the shock unsteadiness. In particular, oscillatory motion of the foot of an incident oblique shock was also found in a DNS study by Pirozzoli and Grasso[13] who attributed the cause to the passage of the low speed coherent structures. The present results are consistent with the studies by Wu and Martin[14] for a compression ramp for which the turbulent structures had a reduced streamwise extent downstream of the shock/boundary-layer interaction. They suggested that this may be due to low-frequency oscillations of the oblique shock which may "chop" the structures.   In the present flow, the reflected oblique shock was observed to undergo oscillations with amplitude on the order of δ_{ref}^{*}.

The streamwise velocity contours in Fig. 4b indicate the scale and shape of the low speed streaks for the case with no flow control device. The lengths of the streaks are on the order of 1000 wall units where the spacing between each streaks are approximately 100 wall units upstream of the shock. This length scale is typical for both incompressible and compressible turbulent boundary layer flow. However, the lengths of the streaks decrease (200~300 wall units) while the spacing widens approximately 15 percent as the flow convects through the shock impingement as shown in the density iso-surface contours of Fig. 4a. Multiple recirculation regions are observed near the shock impingement so that the overall separation bubble is quite three-dimensional and unsteady. Upon insertion of the baseline micro-ramp (BR) as shown in Fig. 4c, the presence of the device causes a horse-shoe vortex which induces flow separation at the foot of the micro-ramp and produces a counter-rotating vortex pair shown by the high speed streaks (yellow and orange) resulting from the entrainment of high-speed fluid to the wall . This is consistent with the findings of Pitt-Ford and Babinsky[15] at much higher Reynolds number. As the vortex pair convects downstream, the high streamwise vorticity fluid breaks up the center of the separation region. This contributes to the recovery of the boundary layer (which was afflicted by unsteadiness of the shock and the adverse pressure gradient) in the form of increased number of high-speed regions.

ii. Vortex Evolution

The spanwise view of the streamwise velocity contour is shown in Fig. 5. The counter-rotating vortex pair mentioned above appears as a pair of vortex tubes when examined just downstream of the μVG trailing edge (left-hand column with arrows indicating the center of the vortex cores). The two primary vortices generated by the BR device are largest in size at the trailing edge and can be seen to locally reduce the boundary layer thickness close to the device due to the entrainment of high speed flow (Fig. 5a). However, the boundary layer thickness increases away from the centerline indicating significant spanwise variation. Also shown in Fig. 5a, are small secondary vortices (in blue) which form due to the corner flow at the ramp's side wall and the bottom floor. These secondary vortices counter rotate against the primary vortex and, as discussed by Ghosh et al.[5], contribute to the rise of the primary vortex from the floor at the inviscid shock location. However, the rise is primarily driven by the upwash generated by the two counter-rotating vortices. The vortices are shown schematically in Fig. 5b superimposed on the velocity field to show their influence. The vortices entrain high-speed fluid downward along the outside edges to thin the boundary layer, but also pull low-speed fluid upwards in between the vortices.   At this point (Fig. 5b), the boundary layer under the vortex pair remains attached and thin despite the shock impingement which is one of the main benefits of using such flow control devices . However, the boundary layer thickness is significantly increased in the outward regions due to flow separation (shown as dark blue region in Fig. 5b).

As the height of the micro-ramp is reduced by half with the HHR geometry, the initial size of the vortex tube pair is reduced proportionally but the vortex core strength is approximately maintained (as is that of the secondary vortices) as shown in Fig. 5c. At the inviscid shock location (Fig. 5d), the primary vortex pair is significantly weakened and does not provide as much centerline thinning as the BR device. However, its lower initial height allows it to have a reduced altitude and decreased intensity appear to have reduced the undesirable thickening at the outer spanwise locations, noted for the BR case.

The micro-ramp reduced in width by half and denoted as HWR yields a pair of primary counter-rotating vortices which are more circular and much closer together in the spanwise direction (Fig. 5e). The reduced width of the micro-ramp also substantially reduces the size of the secondary vortices. Downstream (Fig. 5f), the close proximity of the two counter-rotating vortices causes them to interact more and degrade in their strength as compared to the BR case. This is consistent with trends seen for low-speed subsonic devices which are spaced too close together[7]. The boundary layer thickness (at the centerline) is thinned similar to that seen for the HHR case but with somewhat more spanwise variation.

The split-ramp (SR) is shown in Fig. 5g at the trailing edge. In this case, the primary vortices are circular, similar to the case for HWR, but are separated by a significant spanwise spacing on the order of the device height. At the centerline, there is a high speed flow owing to the channel between the two halves of the device. The increased spanwise spacing allows the vortices to stay closer to the wall and with less dissipation further downstream (Fig. 5h) as compared to the BR case, consistent with the findings by Ashill *et al.*[7]. This spacing leads to an undesirable upwash near the centerline which causes some boundary layer thickening but also results in thinner boundary layer at outward spanwise locations.

Vortex tubes generated by BV and TV yield streamwise velocity fields which are quite similar to the SR case, but with some differences. At the trailing edge location, BV (Fig. 5i) and TV (Fig. 5k) show a substantial internal vortex (shown in green) between the vanes which do not retain the high-speed flow seen for the SR case. At the incident shock location, the similarities of the three cases (Fig. 5h, j & l) are stronger, with the primary difference that the vane cases have vortex cores that are somewhat closer in spanwise spacing and somewhat higher in distance above the floor. This leads to less upwash near the centerline for the vane case (compared to SR), but all three have similarly thin boundary layers at the outward spanwise locations (as compared to the BR, HHR and HWR cases).

The above results indicate that the last three devices tend to have the best downstream performance, which makes SR and TV particularly useful owing to their physical robustness. Generally, the differences between the BV and the TV are quite small, though the TV tends to have a bit less upwash so that its centerline region is somewhat better whereas the BV tend to have somewhat more high-speed (shown in red) fluid pulled down around the vortices.

iii. Flow Separation Area

Flow separation area, defined as the surface region with negative shear stress, can be an important parameter for assessing the μVGs performance, given that a decrease in this area is a desirable feature. The mean flow separation area was obtained using a plane at $y^+=1$ for the six geometries investigated and is shown by the dark color regions in the left-hand column of Fig. 6. The first image shows the solid-wall no-ramp (NR) case where the separation at the shock intersection region is two-dimensional and the accompanying streamwise view of the velocity field (right-hand side column) indicates a thin separation coincident with the oblique shock impact. The left-hand side of baseline ramp (BR) case image shows a pair of thin separation regions related to the streamwise vortices near the centerline.   Downstream of these, in the vicinity of the shock, the flow is seen to stay completely attached while the outer spanwise regions yield a much larger streamwise separation length. The outer spanwise changes are consistent with the BR streamwise velocity contours on the right-hand column and both of these aspects are consistent with Fig. 5b. The half-height micro-ramp case (HHR) yields a similar result but does not completely eliminate the centerline separation, which is attributed to the reduced strength of the primary vortices. The HWR case is similar to the HHR except that there is a fully attached centerline region though not as wide as for the BR case. In general, all three of these cases increased the area of separation beyond the NR cases, as shown in Table 1

The SR, BV and TV cases are substantially different than the BR, HHR, and HWR cases which indicate that the channel region between the vanes dramatically alters the flow. In particular, SR, BV and TV cases yielded separation regions which were much more two-dimensional and similar to the NR case though the indicated effects of the streamwise vortices are shown near the centerline. In general, all three of these devices reduced the area of separation beyond the NR case, with up to a 15% decrease for the TV case (Table 1). This is attributed to the increased size of the primary vortices for these devices, e.g. note in Fig. 5 that the amount of yellow region for the SR, BV and TV cases is much larger than that for BR, HHR and HWR cases.

iv. Vortex Characteristics

To assess the characteristics of the streamwise vortices and their affect on the boundary layer in the vicinity of the shock wave, average values were obtained for various quantities at different downstream distances. In particular, a square spatial averaging window was defined which included a spanwise extent from the centerline of the ramps (z=0) to a position equal to the half-width of the BR height (z=1.46h) and a vertical extent from the bottom floor of the computational domain (y=0) to a similar height (y=1.46h). The limited vertical extent confines the averaging to be primarily within the turbulent boundary layer. Average values of the pressure and turbulent kinetic energy were also obtained in this square averaging window:

$$\frac{P}{P_\infty} = \int_0^{1.46h} \int_0^{1.46h} \frac{p}{P_\infty} \, dy dz \Big/ \int_0^{1.46h} \int_0^{1.46h} dy dz \qquad (11)$$

$$\frac{K}{U_\infty^2} = \int_0^{1.46h} \int_0^{1.46h} \frac{(\overline{u'^2} + \overline{v'^2} + \overline{w'^2})}{U_\infty^2} \, dy dz \Big/ \int_0^{1.46h} \int_0^{1.46h} dy dz \qquad (12)$$

In the first expression, p is the time-averaged pressure at a computational node, P_∞ is the freestream pressure, and P is the spatially-averaged pressure. Likewise, the time-averaged turbulent kinetic energy, given by the sum of the time-average of the fluctuating velocity is used to obtain a spatially-averaged kinetic energy, K. The pressure and kinetic energy averaged using the above equations are shown in Fig. 7 for each of the μVGs in terms of non-dimensional distance from the inviscid shock location defined as $x_{SI}^{**} \equiv (x - x_{SI})/h$. Note that the trailing edge of the μVGs occur at $x_{SI}^{**} = -18$ which is slightly upstream of the y axis in the plot. For the pressure distributions, all the results qualitatively follow the inviscid pressure rise for an oblique reflecting shock as given by the dashed-line. Departures from this dashed-line can be primarily attributed to the viscous effect which causes an upstream influence of the shock and a diffused shock interaction in the streamwise direction. The thickening of the boundary layer and separation before the shock impinges results in a well-established increase in the spatially-averaged pressure. This pressure continues to rise throughout the shock interaction region indicated by the arrow which approximately extends from $x_{SI}^{**} = -10$ to 10 over a distance that is consistent with the length of the separation bubbles. It can be noted that the BR, HHR and HWR cases are all nearly identical (Fig. 7a), but that the SR, BV and TV cases tend to have a less diffused pressure rise (Fig. 7b). This can be attributed to a reduction in their overall streamwise separation bubble length in comparison. The spatially-averaged turbulent kinetic energy, K, shown in Fig. 7c & d for all the μVGs cases is somewhat higher than that for traditional supersonic boundary layers at $x_{SI}^{**} = -15$ owing to the wakes from the devices since this position is 3h downstream of their trailing edge. However, the impact of the shock-wave enhances turbulence such that the kinetic energy is increased by nearly three-fold. The oblique shock DNS results of Pirozzoli and Grasso[13] (without a flow control device) similarly showed a 2.7 increase in the mean turbulent kinetic energy at the shock location in comparison with the upstream condition. This was attributed to the strong mixing layer at the separation bubble, as well as the shock oscillations. The BR case has the highest peak value of K at x_{SI}^{**} of about zero which may be related to the larger and more complicated separation region for this case (as well as that for HHR and HWR). The lower intensities for the SR, BV and TV cases can thus may be related to the smaller overall area of their separation bubbles compared with those of the other three devices (consistent with Fig. 6 and Table 1). Further downstream at $x_{SI}^{**} = 26$, it is interesting to note that the BR, HHR and HWR cases have lower turbulence levels than those of the other three devices. The reason for this is less clear but may be due to an increased persistence of the unsteady streamwise vortices within the boundary layer.

The streamwise variation of ω_{max} (peak vorticity within the vortex core which is normalized by the free-stream velocity and the height of the baseline ramp) with respect to streamwise-distance is shown in Fig. 8a & b. The streamwise-distance is referenced to the generator trailing-edge and normalized by the generator height as: $x_{TE}^{**} \equiv (x - x_{TE})/h$ (note that the theoretical shock impinges at $x_{TE}^{**} = 18$). At $x_{TE}^{**} = 3$ (equivalent to $x_{SI}^{**} = -15$), magnitude of ω_{max} is highest for the most cases (Fig. 8a) since this position is close to the μVG trailing edges. Through the shock-wave the strength of the vorticity decays rapidly. This can be attributed to the high rate of mixing evidenced by the large increase in kinetic energy at this point and is consistent with the flow visualization of

Fig. 4c. Reducing the height (HHR) caused a dramatic reduction in the initial vorticity which can be attributed to a smaller surface area for flow turning but also an increased immersion in the boundary layer, so that less of the high speed fluid was affected by the device. However, reduction in the width (HWR) gave higher initial vorticity which maybe caused by decreased ramp side angle allowing the vortices to form quickly. As seen earlier in Fig. 5, HWR case yielded an even circular structure at the trailing edge of the device whereas the vortex formation is still in the transitional stage with other devices yielding an oval-like shape. In the shock interaction region (whose span is indicated by the arrow), there are large variations in the decay rate due to different interactions of the vortices with the shock. However, far downstream of the shock impingement (x_{TE}^{**} =44), all three of these ramps reduced to similar vorticity levels. This is in contrast to the more profound differences noted at x_{TE}^{**} =18 (near the shocks) in this Figure and in Fig. 5b, d & f. Thus, the geometric differences are mostly lost far downstream of the trailing edge of the generators and the shock interaction.

The split ramp and thick vane cases (SR and TV) showed higher initial vorticity compared to the baseline ramp case (Fig. 8b), while the baseline vane case yielded a lower strength. Furthermore the streamwise vorticity for the SR, BV and TV cases were more robust to the shock strength yielding higher levels than that of the BR case near and downstream of the interaction (x_{TE}^{**} >18). This may be partially attributed to the slightly reduced altitude of the vortex core for these cases as compared to the BR case. However, the primary reason for the persistence through the shock may be the significantly increased lateral spacing, which reduced the vortex-vortex interaction and the vortex-shock distortion. In addition, this may be due to a more stable flowfield for the separated vortices, which is consistent with reduced kinetic energy for the vane-type devices.

The trajectories of the vortex pair is approximated by the position of the ω_{max}, Y and Z, which are the normal and spanwise positions respectively. The Y trajectories from the numerical results initially follow the Ashill *et al.*[7] experimental data for a single device which has no shock at low Mach number flow with zero pressure gradient, as shown in Fig. 8c & d. The vortex pair trajectories from the low-speed Ashill *et al.*[7] experiments continue to rise while the trajectories in the present simulations contain a significant descent in the shock interaction region. This is attributed primarily to the impinging shock. The impinging shock tilts the vortex paths downward but afterwards they tend to recover the lifting effect similar to the subsonic case[16]. As expected, HWR/HHR has the highest/lowest distance above the floor which is consistent with the results seen in Fig. 5. However, SR and the micro-vanes maintained a low profile for most of its path due to the spacing between the vortex pair which reduced the up-wash effects (Fig. 8c & d). A schematic of the vortex pair trajectory and the streamlines of the averaged MILES are shown in Fig. 9a & b for BR, which suggests that a vortex tube traveling at higher distance above the floor will be more affected by the shock waves since it will be more directly exposed to gas dynamic waves. As shown in Fig. 9c & d for BR and TV respectively, the streamlines close to the centerline initially collapses closer just downstream of the device wake (a triangular blue region) after which they slightly expand in the shock interaction region. The reason for this expansion is not clear but may be related to a sudden enlargement of the vortex due to the shock interaction. It is well known that the vortices subjected to sufficiently strong adverse pressure gradient develops "vortex-breakdown" or "vortex-bursting", as discussed by Delery[17] for a variety of speed regimes. Once a bursting occurs, the diameter of the vortical structure rapidly expands with significant changes in the velocity profile. Similar behavior was observed in the study by Smart *et al.*[18] for vortex penetrating a shock surface where the vortex diameter expanded to nearly double the size of that upstream of an oblique shock. Thus dilation of the vortex core may be the main cause of the diverging trajectory of the vortex pair near the shock location. In the case for SR, BV and TV, the vortices are initially further away from each other in the spanwise direction (Fig. 8f) due to the spacing between the each component of the device which is consistent with the arrow positions in Fig. 5. Since these vortices are further apart, they do not undergo significant contraction upstream of the shock interaction. Once entering the interaction, the streamlines neck-in due to the low-velocity high-pressure separated regions on the sides (shown in blue) and perhaps are less likely to burst due to their increased spacing from each other, as shown in Fig. 8e & f.

The correlation of the vortex strength represented by the circulation at 5h down stream for the µVGs is shown in Fig. 10a, agrees within the experimental uncertainties with the curve fit data[16]. The circulation is computed around the edges of the same averaging window used in Equation 11 and 12. The numerical results occur at small h^+ values due to low Reynolds number flow. The streamwise vorticity decay with distance is shown in Fig. 10b, where the vorticity is normalized by that at x_{TE}^{**} =5. All the present results show a rapid decay within the shock interaction region, while the low-speed subsonic result from a circulation profile indicate a slow but consistent decay rate with downstream distance.[16] In contrast to the ramps devices, the vane-type devices had stronger persistency of vorticity

strength through the interaction and maintained the strongest level at x^{**}_{TE} =44. This is attributed to the large initial spacing between the vortex pair which reduces vortex interaction and shock distortion, as seen in Fig. 8f.

v. Spanwise Distribution of Performance Parameters

The impact of the micro-vortex generators at the measuring plane, MP shown in Fig. 2, were investigated using as the basis on stagnation pressure recovery factor, α, displacement thickness, δ^*, momentum thickness, θ, and the incompressible shape factor which are defined as:

$$\alpha = \int_0^{y_{max}} (P_o / P_{o,\infty})dy \tag{13}$$

$$\delta^* = \int_0^{y_{max}} (1 - U / U_\infty)dy \tag{14}$$

$$\theta = \int_0^{y_{max}} U/U_\infty (1 - U/U_\infty)dy \tag{15}$$

$$H = \delta^* / \theta \tag{16}$$

In this expression, $P_{o,\infty}$ is the stagnation pressure at freestream, y_{max} is the maximum height to avoid interference of the expansion wave emanating the upper wall (=23δ_{ref}^*), these parameters are plotted as a function of spanwise distance in Fig. 11.

The stagnation pressure recovery factor for the BR case indicated large deficits in the centerline wake region due to the drag of the flow control devices. The HHR and HWR, having smaller dimensions, had a lesser effect (Fig. 11a). However, BV and TV increase the deficit in the wake region which may be due to stronger transformation of streamwise energy into vorticity as shown in Fig. 11b. Despite the losses in the wake region, the micro-vanes and other variation of the micro-ramps (HHR, HWR, SR) had much improved results at the outward regions. This may be due to the initial spanwise spacing of the primary vortex pair which allowed them to be less distorted by each other and diffused by the shock. Consequently, the spanwise average values were higher than the BR case as shown in Table 1. Although the resulting values reveal that the losses due to the μVGs were greater than for the case with no flow-control device, HHR had the highest recovery factor shown in Table 1.

Likewise, the displacement thickness distribution, shown in Fig. 11c & d, displays the large wakes of the μVGs at the center region where SR, BV and TV had the most impact. Despite the improvements in the displacement thickness in the outward spanwise region, especially for BV and TV shown in Fig 11d, the increase in the spanwise average thickness were greater than that for the losses seen in the pressure recovery as shown in Table 1. The average displacement thickness normalized by that with no flow-control device for TV gave 13% increase where HWR had the least increase.

The shape factor in Fig. 11e & f are presented as increments which are referenced to the shape factor measured at the μVG position without the device and shock. Peaks in the center region for the shape factors, as shown in Fig. 11e & f, are consistent with the wake deficit shown in both the displacement thickness and the stagnation pressure recovery factor though the spanwise average results were similar to NR case shown in Table 1. The overall shapes from BV and TV results have similarities with the measured incompressible shape factors of Ashill *et al.*[7] with adverse pressure gradient. However, the overall reductions in the shape factor for the experiments[7] are greater than the numerical results indicating much improved performance which maybe due to the higher Reynolds number.

IV.   Conclusions

Several different types of μVGs with various dimensions and shapes for supersonic boundary layer flow control are studied using Monotone Integrated Large Eddy Simulation (MILES). A third-order upwind spatial scheme with a second-order approximate factorization scheme using baseline structured grid generated flow solutions that were in good agreement with the experimental data. A special 'rescale-recycle' algorithm for compressible flows is used to generate turbulent inflow conditions which reduce computational cost by eliminating the need to compute boundary layer flows from the leading edge of the flat plate.

Shock interaction with the boundary layer produces substantial break-up in the turbulent structures, resulting in smaller aspect ratios just downstream of the shock impingement which may be caused by the unsteadiness of the reflecting shock interacting with the low-speed coherent structures. Further downstream, the structures tended to pre-shock characteristics. Similar results were found when a micro-ramp was present but their counter-rotating vortices dominated the streamwise vorticity in the vicinity of the shock interaction. The simulations showed that strong streamwise vorticity is generated by the µVGs and this vorticity helps to entrain high momentum from the upper boundary layer to the wall. This high momentum generated by the µVGs contributes to reducing or breaking up the flow separation region induced by the shock. The micro-vane and the hybrid devices, namely the "thick vane" and the "split ramp", had the most impact in reducing the flow separation due to the persistence of strong streamwise vortices through the shock interaction. This persistence can be related to the increased spanwise spacing between the two primary streamwise vortices at their point of formation which also helped to reduce the local turbulence intensity and dissipation levels compared to that seen for the micro-ramp case. The impinging oblique shock influences the trajectories of the vortex pair so that its path normal to the wall turns downward at the shock impingement and recovers at downstream location. The spanwise trajectories of the vortex pair are also affected by the shock which induces the vortex diameter to expand and causes the vortex pair to repel from each other.

Despite the drag penalty due to the presence of the µVGs, where BR gave the most loss in the stagnation pressure recovery, incompressible shape factors were reduced in most cases indicating a healthier boundary layer. However, the flow disturbance caused by the µVGs increased the displacement thickness with the micro-vanes having higher values than the micro-ramps due to strong streamwise vorticity. Such events may correlate to the higher peaks of turbulent kinetic energy and rapid streamwise vorticity decay at the shock region.

V.   Acknowledgements

References

[1]Loth, E. Smart Mesoflaps for Control of Shock Boundary Layer Interactions, *AIAA 2000-2476.*

[2]McCormick, D. C. Shock/Boundary-Layer Interaction Control with Vortex Generators and Passive Cavity, *AIAA Journal*, **31**, (1), pp 91-96.

[3]Holmes, A. E., Hickey, P. K., Murphy, W. R., Hilton, D. A. The Application of Sub-Boundary Layer Vortex Generators to Reduce Canopy Mach Rumble Interior Noise on the Gulfstream III, *AIAA 87-0084.*

[4]Anderson, B., Tinapple, J. and Surber, L. Optimal Control of Shock Wave Turbulent Boundary Layer Interactions Using Micro-Array Actuation, *AIAA 2006-3197.*

[5]Ghosh, S., Choi, J. and Edwards, J. RANS and Hybrid LES/RANS Simulations of the Effects of Micro Vortex Generators Using Immersed Boundary Methods, *AIAA 2008-3728.*

[6]Lee, S., Loth, E., Wang, C. and Kim, S. LES of Supersonic Boundary Layers mVG's, *AIAA 2007-3916.*

[7]Ashill, P. R., Fulker, J. L. Hackett, K. C. Studies of flows induced by Sub Boundary layer Vortex Generators (SBVGs), *AIAA 2002-0968.*

[8]Urbin, G., Knight, D., and Zheltovodov, A.A. Compressible Large-Eddy Simulation using Unstructured Grid: Supersonic Turbulent Boundary Layer and Compression Corner, *AIAA 99-0427.*

[9]Holst, T. L. On Approximate Factorization Scheme for Solving the Full Potential Equation, NASA TM 110435.

[10]Urbin, G., Knight, D., and Zheltovodov, A.A. Large-Eddy Simulation of a Supersonic Compression Corner, Part I, *AIAA 2000-0398.*

[11]Lund, T., Wu, X., and Squires, K. Generation of Turbulent Inflow Data for Spatially-Developing Boundary Layer Simulations, *Journal of Computational Physics*, **140**, (2), pp 233-258.

[12]Cantwell, B. Organized Motion in Turbulent Flow, *Annual Review of Fluid Dynamics 1981*, **13**, pp457-515.

[13]Pirozzoli, S., Grasso, F. Direct numerical simulation of impinging shock wave/turbulent boundary layer interaction at M=2.25, *Physics of Fluids*, 2006, **18**, (6), Article 065113.

[14]Wu, M., Martin, P. Direct Numerical Simulation of Supersonic Turbulent Boundary Layer over a Compression Ramp, *AIAA Journal*, 2007, **45**, (4), pp 879-889.

[15]Babinsky, H., Li, Y., Pitt Ford, C., Microramp Control of Supersonic Oblique Shock Wave / Boundary Layer Interactions, *AIAA Journal*, **47**, (3), pp 668-675

[16]Ashill, P. R., Fulker, J. L., Hackett, K. C. A Review of Recent Developments in Flow Control, *The Aeronautical Journal*, 2005, **109**, (1095), pp 205-232.

[17]Delery, J. M. Aspects of Vortex Breakdown, *Progress in Aerospace Sciences*, 1994, **30**, pp 1-59.

[18]Smart, M.K., Kalkhoran, I. M., Popovic, S. Some Aspects of Streamwise Vortex Behavior during Oblique Shock Wave/Vortex Interaction, *Shock Waves*, 1998, **8**, p. 243-255.
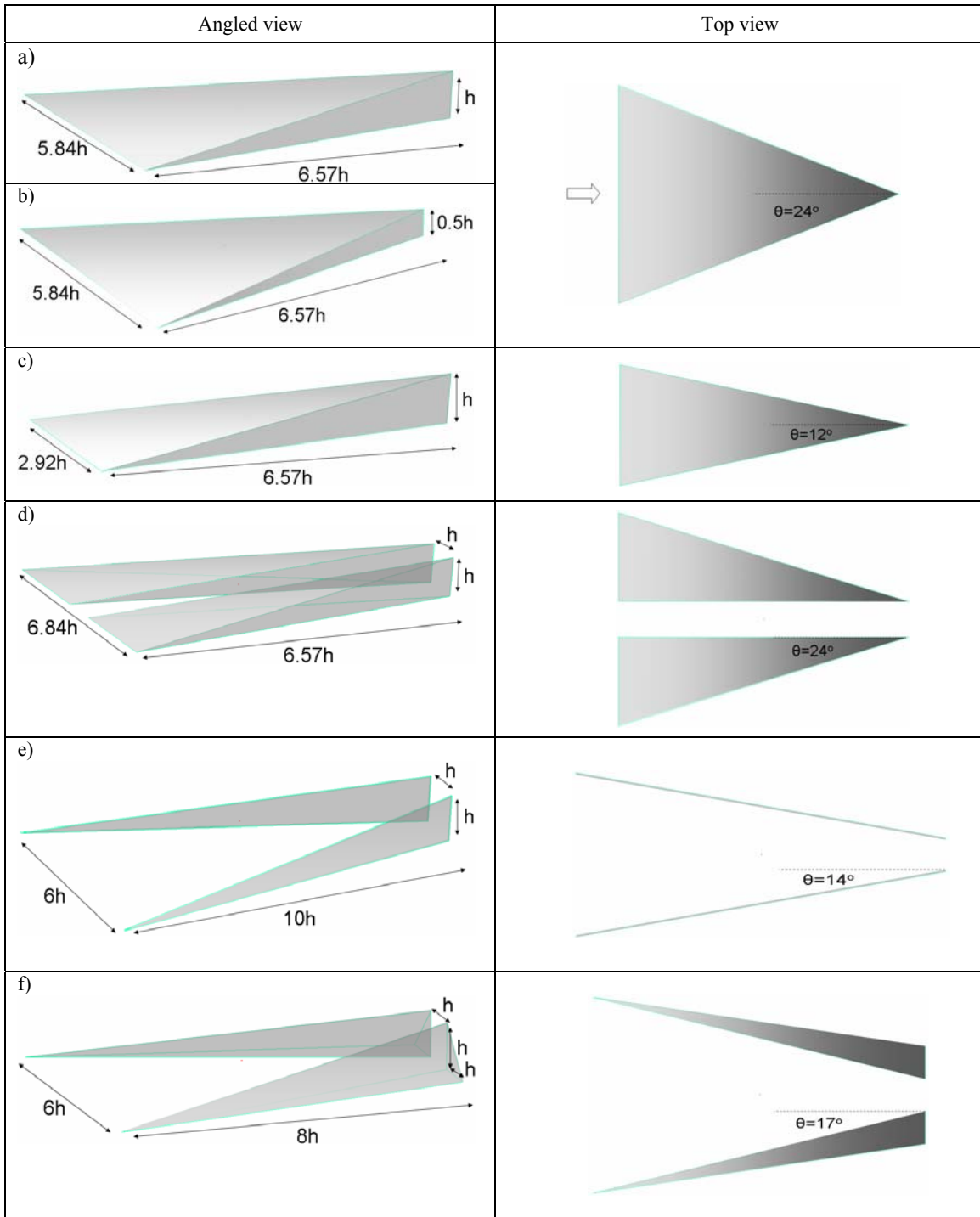
Angled view	Top view
a) 5.84h 6.57h h	θ=24°
b) 5.84h 6.57h 0.5h	
c) 2.92h 6.57h h	θ=12°
d) 6.84h 6.57h h h	θ=24°
e) 6h 10h h h	θ=14°
f) 6h 8h h h h	θ=17°

Fig. 1 Various types of µVGs with length and width scaled with the height (h) where the spacing between the centerlines of the adjacent µVGs is 7.5h : a) baseline ramp (BR), b) half height ramp (HHR), c) half width ramp (HWR), d) split ramp (SR), e) baseline vane BV, f) thick vane (TV)

a)

8° wedge

86.3 δ_{ref}^*

$y^+ = 0.9$

L=312 δ_{ref}^*

57 δ_{ref}^*

δ_{ref}^*

86.2 δ_{ref}^*

23.7 δ_{ref}^*

MP

b)
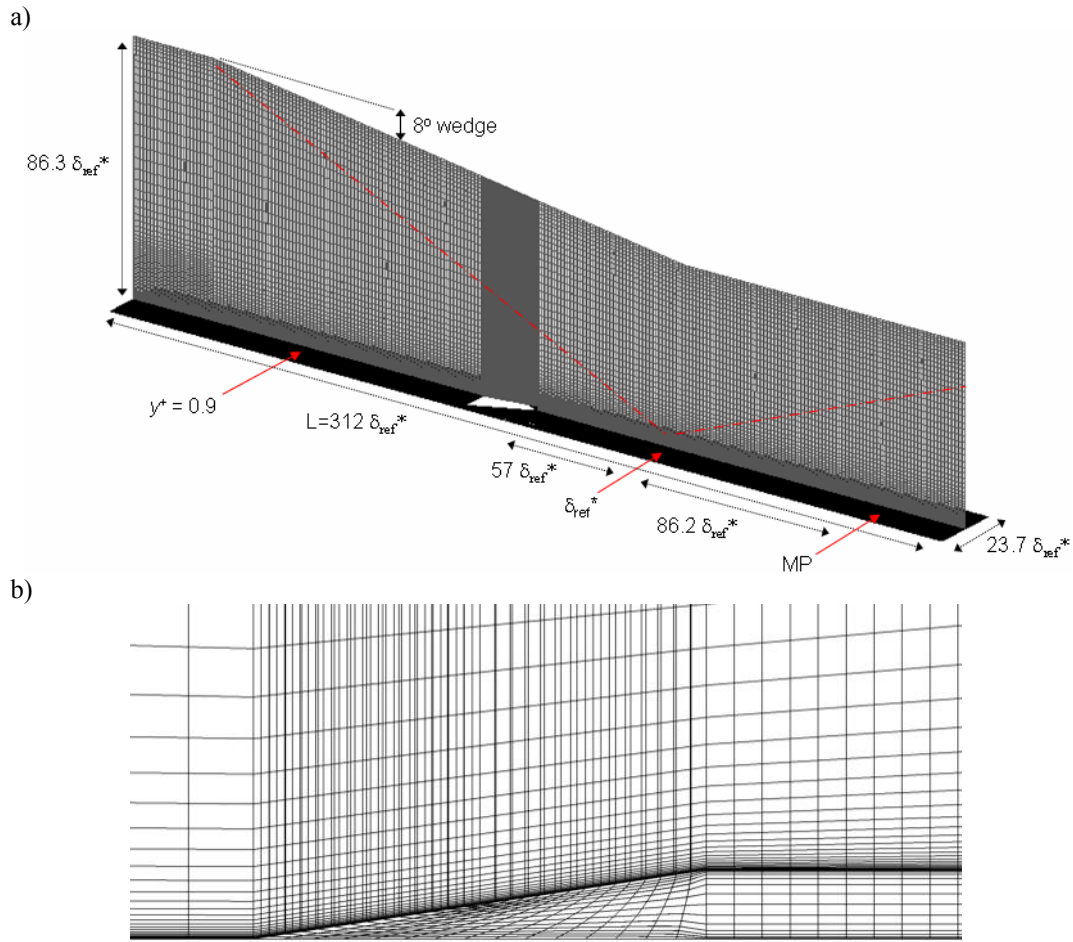
Fig. 2 Computational grid a) at z=0 with the domain dimensions and b) a side view of the µVG at z=11.85δ_{ref}^*
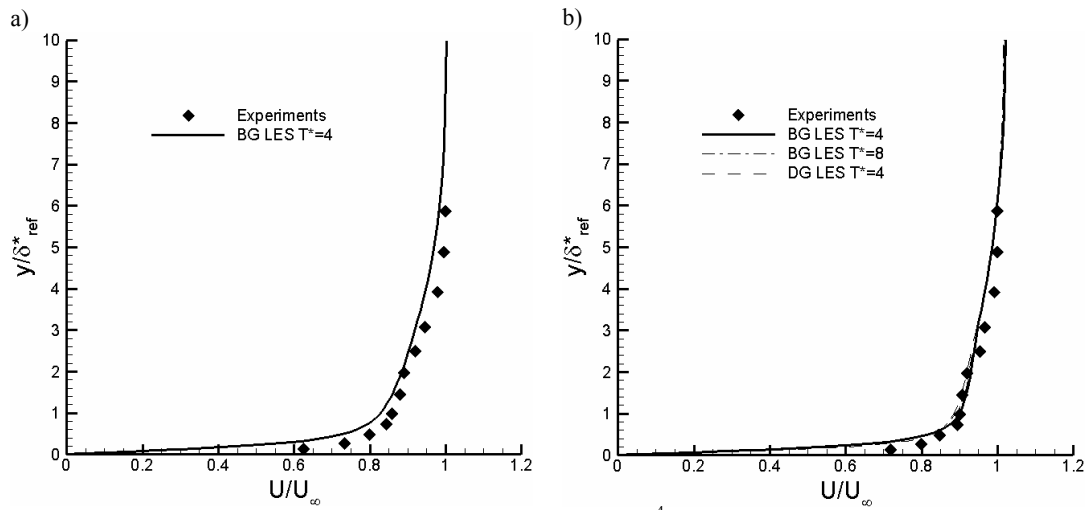
Fig. 3 Streamwise velocity profile compared with experimental data[4] at MP for a) NR and b) BR where results for the baseline grid (BG), the dense grid (DG) and two different averaging time-scales are compared
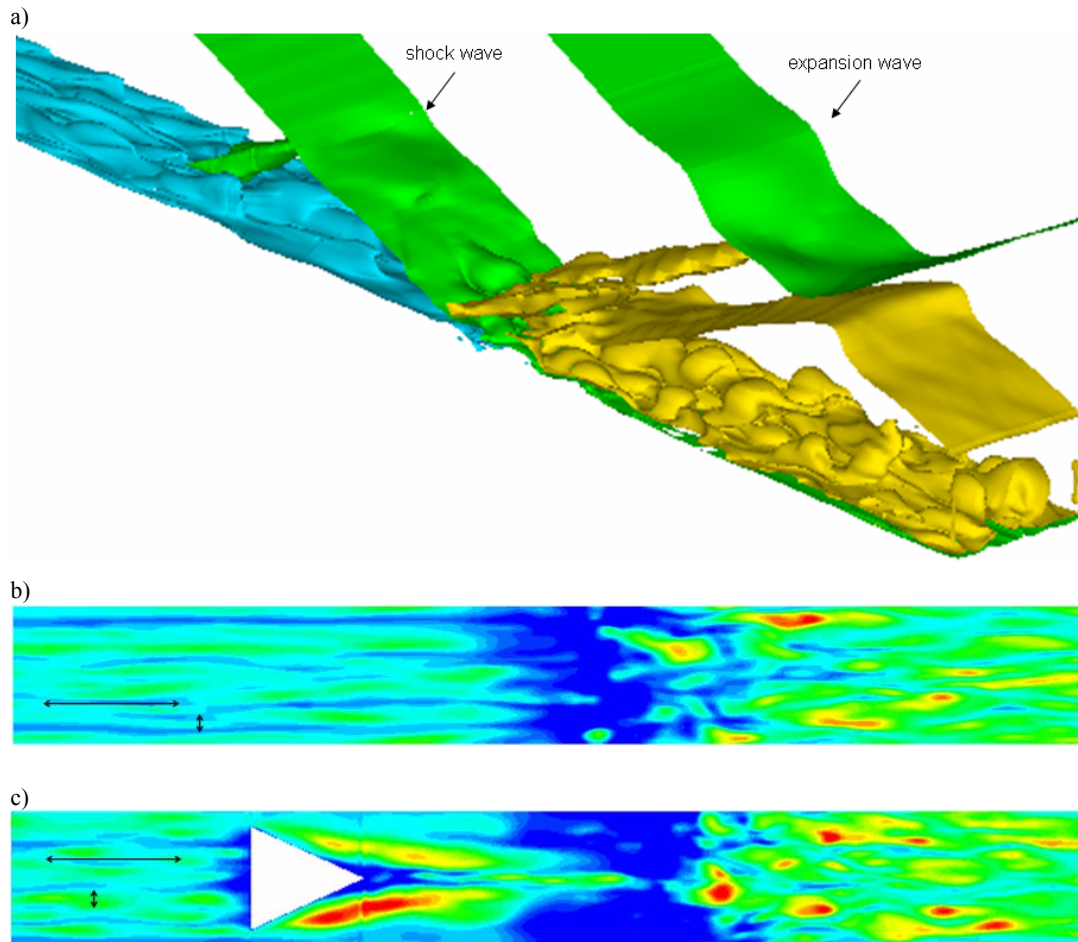
a)

shock wave

expansion wave

b)

c)

Fig. 4 Flow visualization of oblique shock interaction: a) density iso-surface for NR, b) velocity contours at y^+=5 for NR and c) velocity contours at y^+=5 for BR showing reference lengths of 1000 streamwise wall units and 100 wall spanwise wall units.
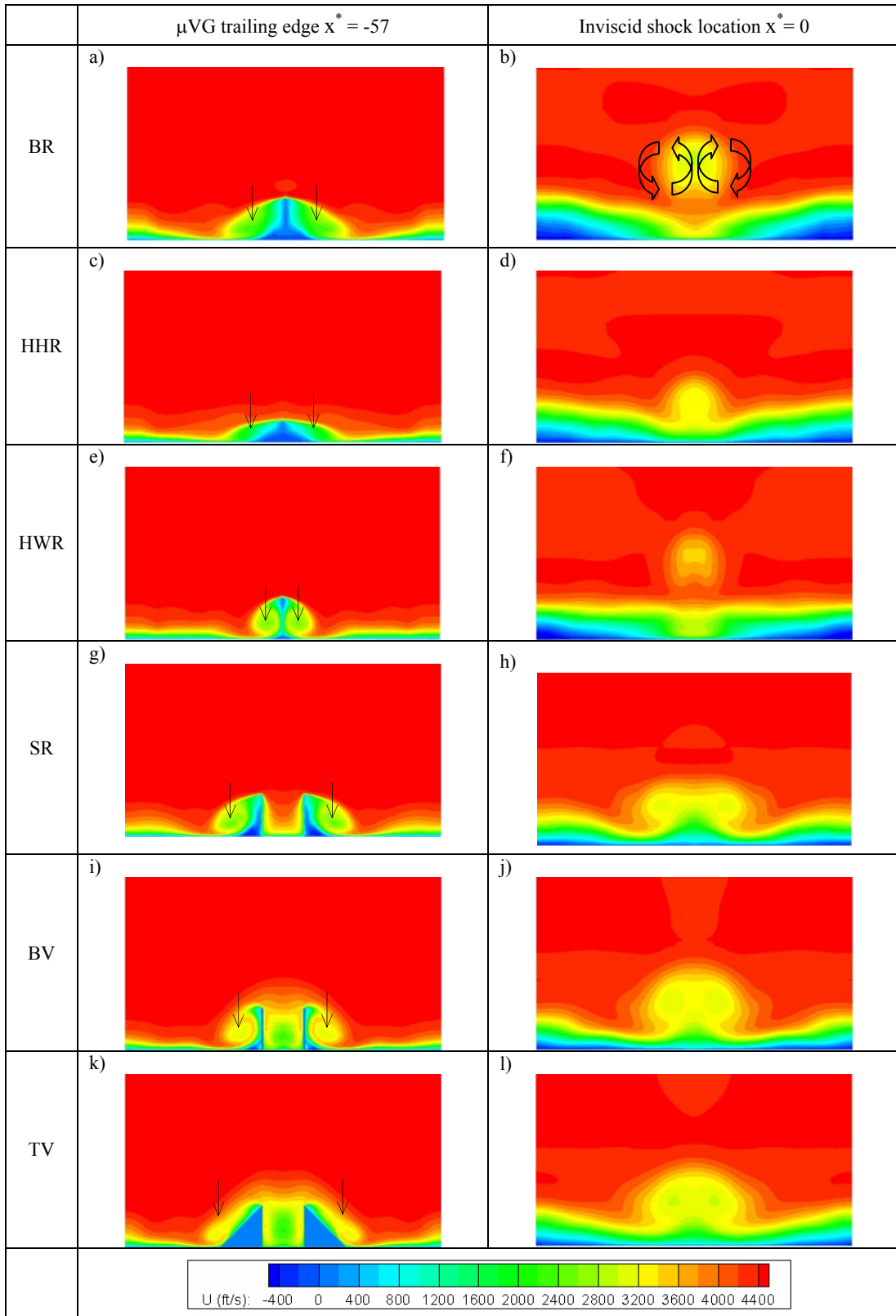
Fig. 5 Cross-sections of time-averaged (T^*=4) streamwise velocity contour at the trailing edge of µVGs ($x^* = -57$ with the center of the vortices are indicated by the arrows) and the inviscid shock location ($x^* = 0$)

	a) Spanwise view at $y^+ = 1$ (near floor)	b) Streamwise view at $z^* = 11.8$ (span edge)
NR		
BR		
HHR		
HWR		
SR		
BV		
TV		
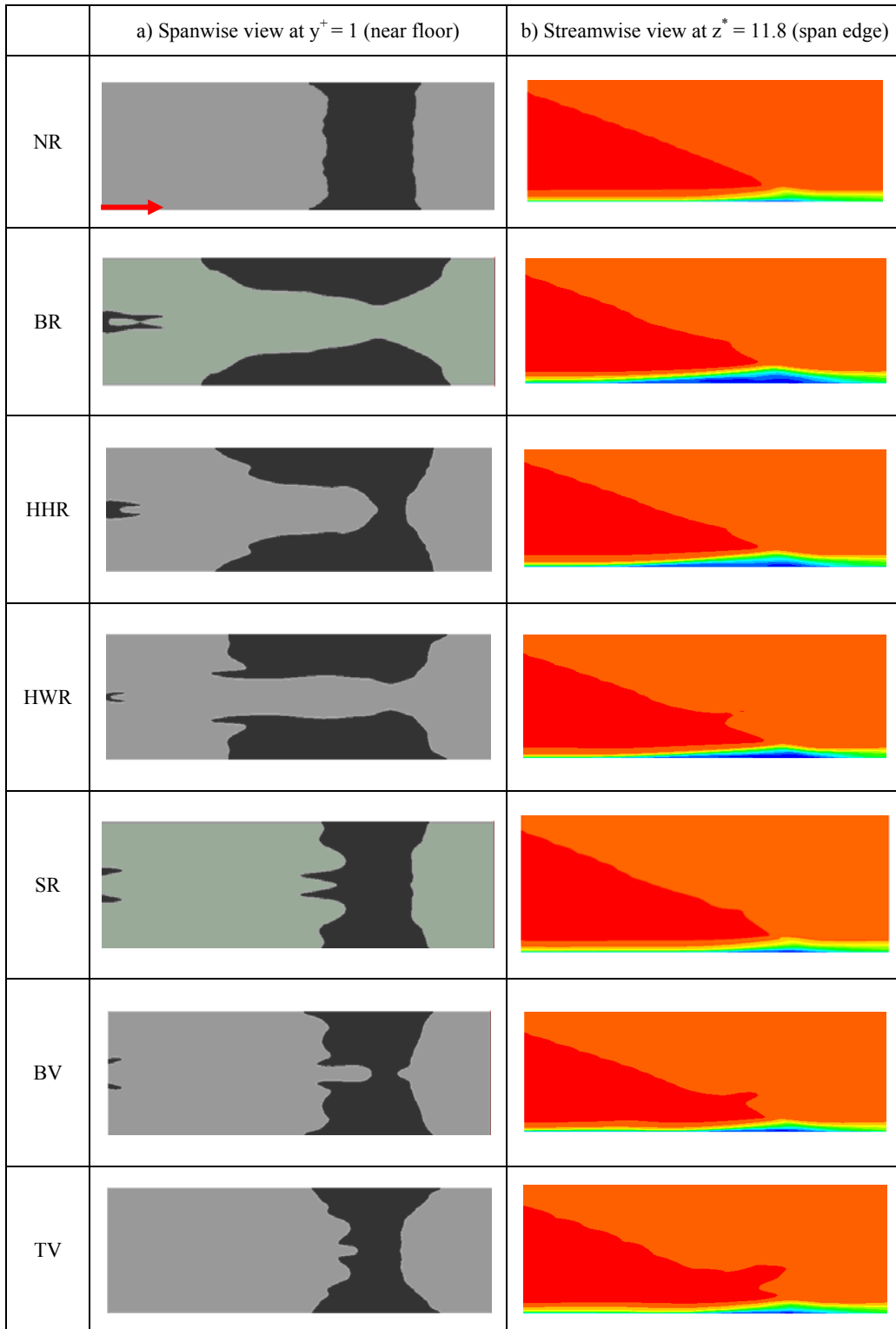
Fig. 6 Time-averaged streamwise velocity contour for a) spanwise view of flow separation region shown in dark for negative wall shear stress at $y^+=1$ and b) streamwise view showing the oblique shock and the separation bubble (blue region) for $x^*=-57$ to 19 at a spanwise location of $z^*=11.8$ (consistent with the red arrow in Fig. 6a)
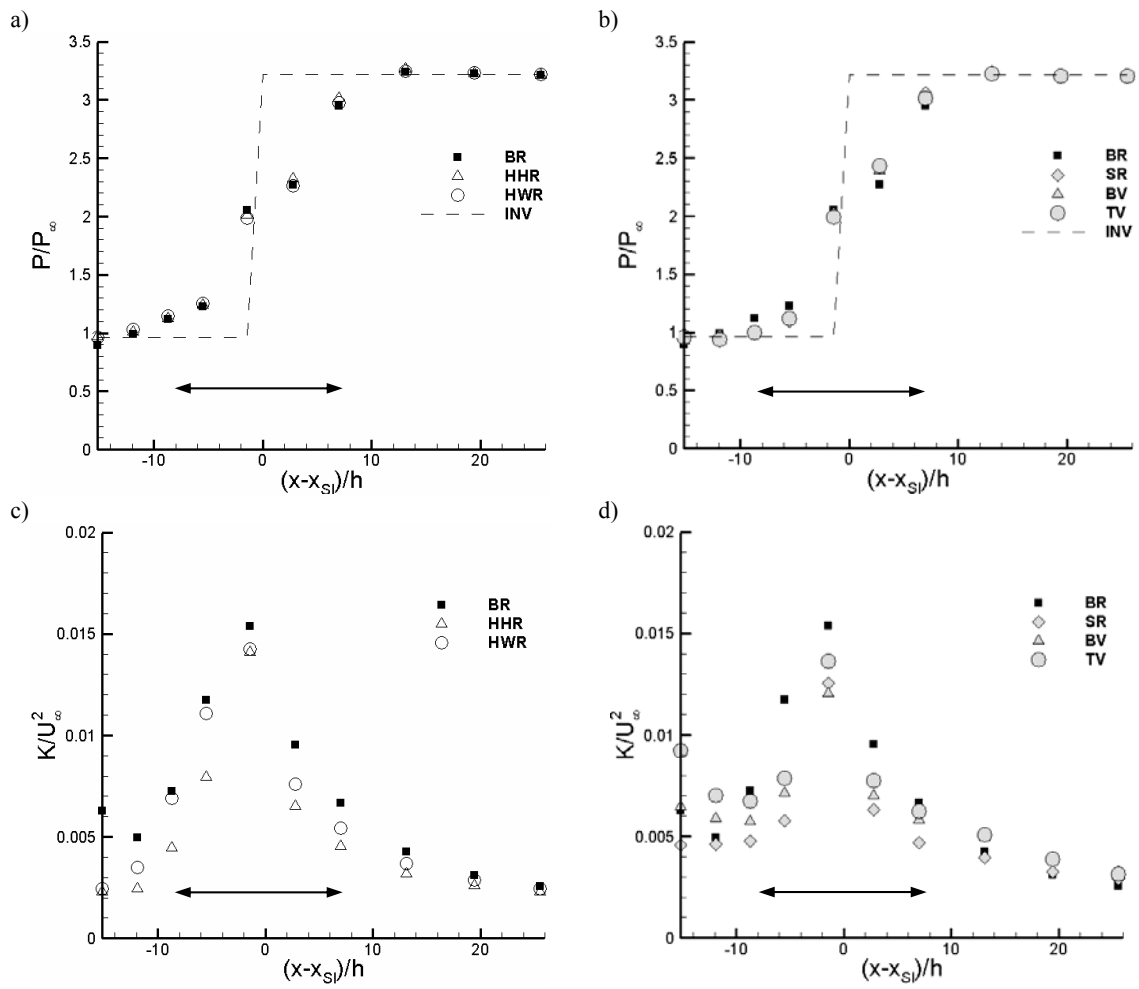
Fig. 7 Time-spatially averaged (for $T^*=4$ for $y^*=0$ to 4.66 and $z^*=0$ to 4.66) values for pressure and turbulent kinetic energy at discrete streamwise locations. Arrows indicate the SBLI regions.
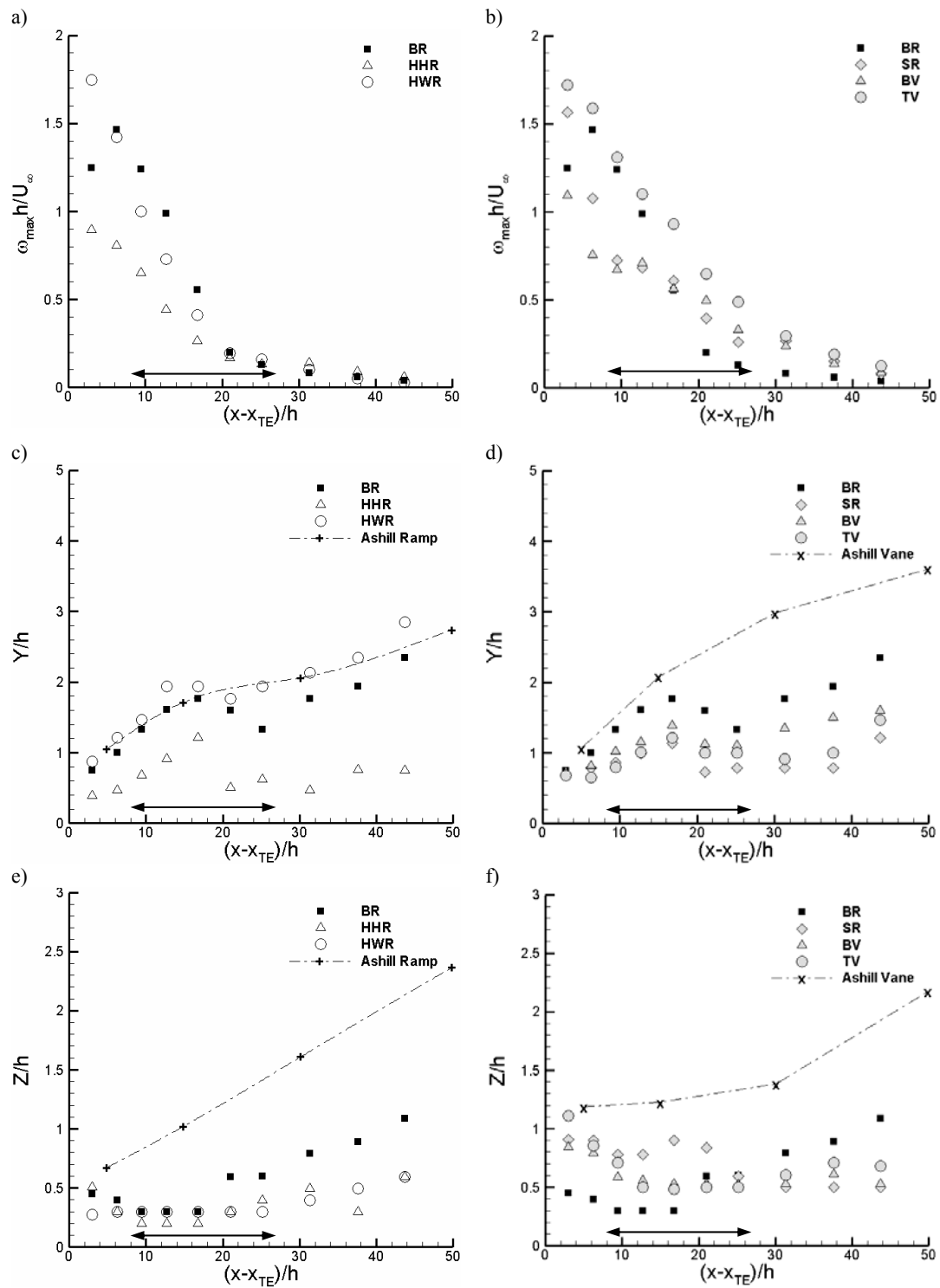
Fig. 8 Temporally and spatially averaged (same as Fig. 7) values for streamwise vorticity and the spatially averaged center that represents the path of the vortex pair for each μVGs. Arrows indicate the SBLI region.
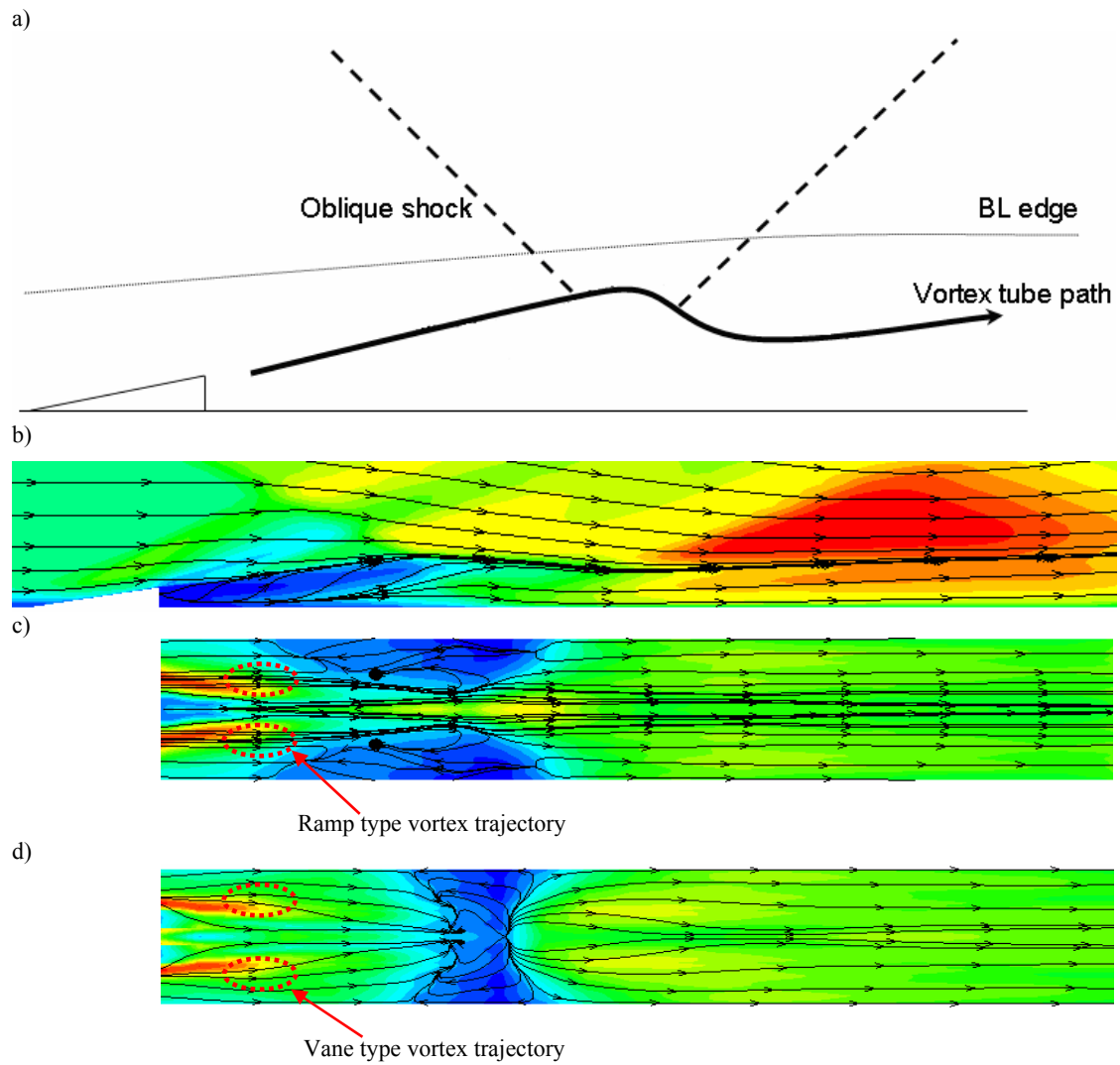
a)

Oblique shock

BL edge

Vortex tube path

b)

c)

Ramp type vortex trajectory

d)

Vane type vortex trajectory

Fig. 9 Side view a) schematic of transverse path of the vortex tube with respect to the boundary layer (BL) edge with the oblique shock interaction, b) averaged density contour of BR case, top view of the streamwise velocity contours at $y^+=5$ for c) BR and d) TV where the streamlines show the approximate trajectories of the primary vortices.
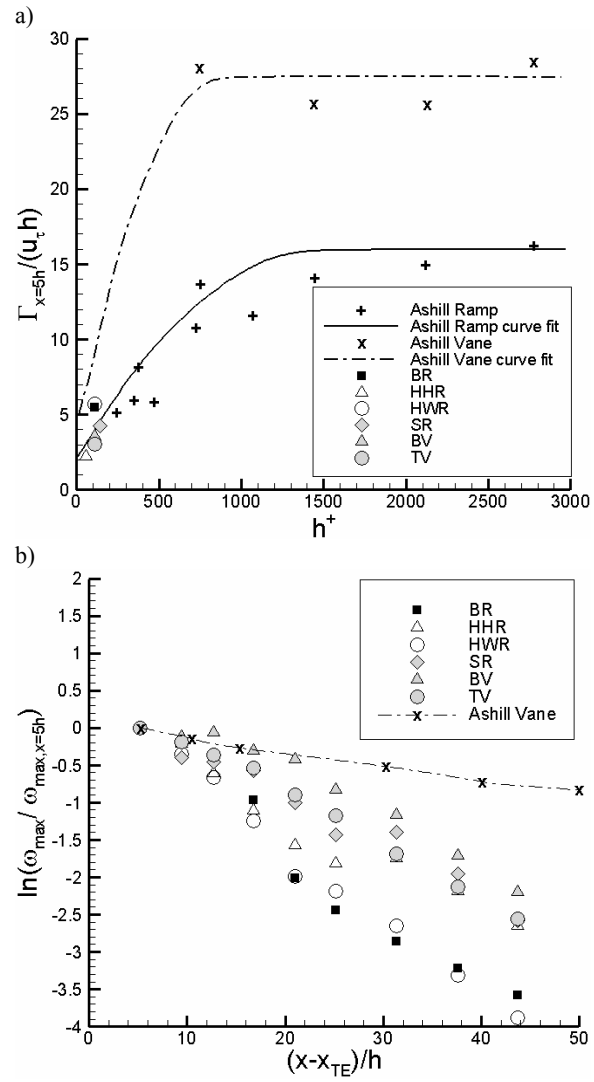
Fig. 10 Correlation of a) circulation of various μVGs at 5h downstream with the device height in wall units and b) decay of vortex peak strength with downstream distance.
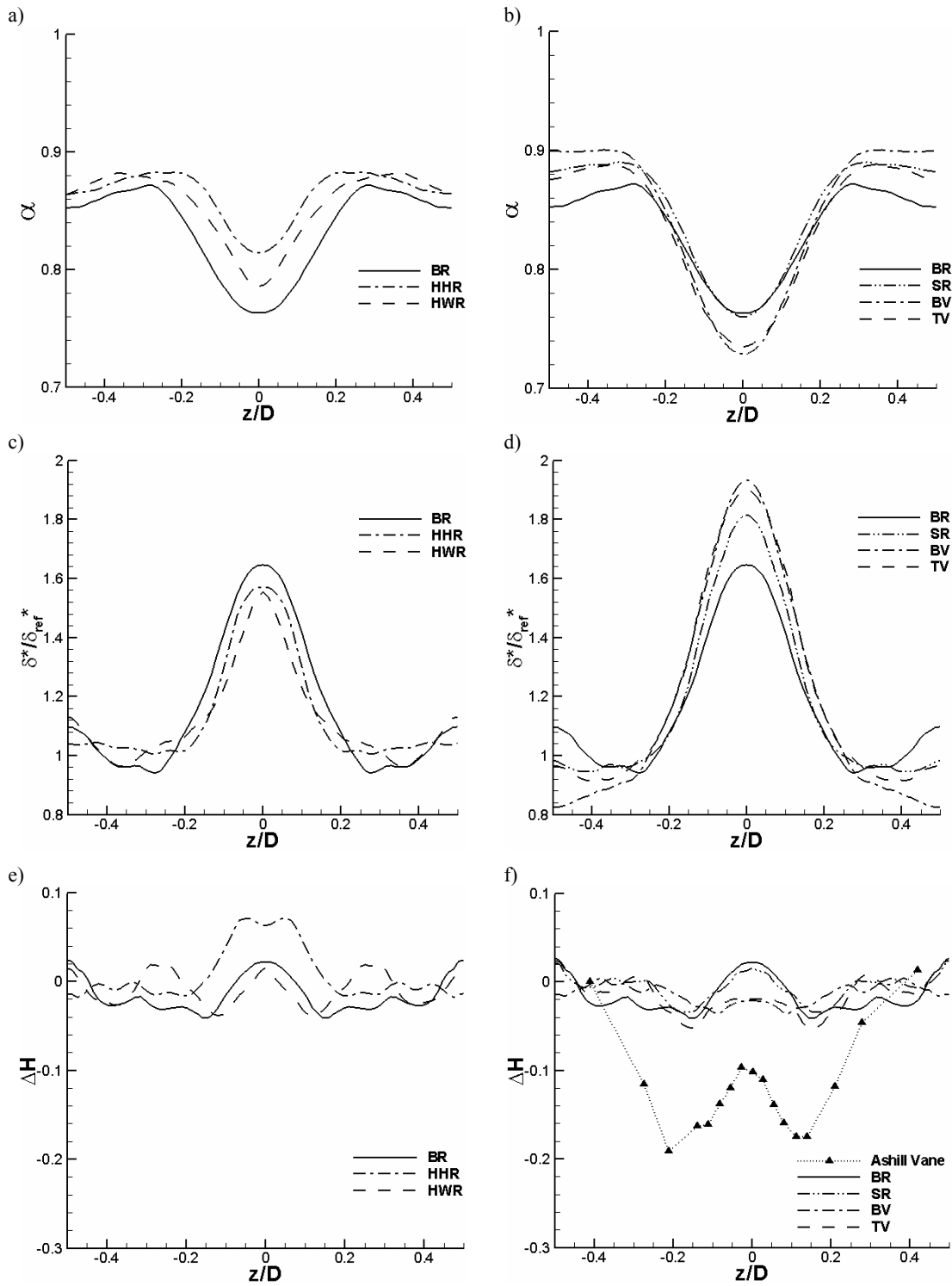
Fig. 11 Spanwise distribution of stagnation pressure recovery, displacement thickness and incompressible shape factor for various μVGs, where $\delta_{NR}*/\delta_{ref}* = 1.07$, $\alpha_{NR} = 0.80$ and $H_{NR} = 1.25$. The incompressible shape factor from Ashill *et al.*[7] data for a baseline micro-vane (Ashill Vane), which has the same dimensional scaling as Fig. 1e, is compared with the present MILES result.

Table 1 Spanwise averaged performance parameters for different μVGs with $A_{\text{sep NR}}=8.01D\delta_{\text{ref}}^{*}$

	BR	HHR	HWR	SR	BV	TV
$\alpha/\alpha_{\text{NR}}$	0.95	0.99	0.98	0.97	0.97	0.96
$\delta^{*}/\delta^{*}_{\text{NR}}$	1.08	1.06	1.05	1.10	1.10	1.13
H/H_{NR}	0.99	1.02	1.01	1.00	0.99	0.99
$A_{\text{sep}}/A_{\text{sep NR}}$	1.29	1.39	1.50	0.97	0.99	0.85